Reconfigurable Polarizer Based on Bulk Dirac Semimetal Metasurface

Yannan Jiang, Jing Zhao and Jiao Wang *

Guangxi Key Laboratory of Wireless Wideband Communication & Signal Processing, Guilin 541000, China; ynjiang@guet.edu.cn (Y.J.); zj_sunday@163.com (J.Z.)

* Correspondence: wangjiao@guet.edu.cn

Abstract: In this paper, we propose a reflective polarizer in terahertz regime, which utilizes the Bulk-Dirac-Semimetal (BDS) metasurface can be dynamically tuned in broadband. The proposed polarizer is capable of converting the linear polarized wave into the circular polarized or the cross polarized waves by adjusting the Fermi energy (E_F) of the BDS. In the frequency range of 0.51 THz and 1.06 THz, the incident linear polarized wave is converted into a circular polarized wave with an axial ratio (AR) less than 3 dB when $E_F = 30$ meV. When $E_F = 45$ meV, the cross-polarization conversion is achieved with the polarization conversion ratio (PCR) greater than 90% in the band of 0.57−1.12 THz. Meanwhile, the conversion efficiencies for both polarization conversions are in excess of 90%. Finally, the physical mechanism is revealed by the decomposition of two orthogonal components and the verification is presented by the interference theory.

Keywords: reconfigurable polarizer; tunable metasurface; broadband; Bulk-Dirac-Semimetal

1. Introduction

In recent years, terahertz (THz) technology has developed rapidly in many fields, such as sensing [1], imaging [2] and radar [3] because terahertz waves have very low photon energy, strong penetrability, and obvious characteristic absorption peaks, making terahertz technology show significant research value and great prospects in material detection, security inspection, military, and wireless communications. The increasing demand of unoccupied and unregulated bandwidth for wireless communication systems inevitably leads to the extension of operation frequency toward the lower THz frequency range. THz communication, with a higher carrier frequency, allows for fast transmission of huge amounts of data as needed for new emerging applications [4]. However, the practical application of THz technology has great limitations due to the lack of THz devices such as absorber, sensor, and polarizer. As a basic THz device, polarizer, controlling and manipulating the polarization of THz waves can convert the linear polarization waves into circular polarization waves or cross polarization waves [5]. Conventionally, the THz polarizer is designed by using the techniques of birefringent material [6], photonic crystals [7] or the grating [8]; nevertheless, these techniques suffer from demerits such as bulky configurations and low efficiency.

Metamaterials, with the feature being easy to integrate, have enabled the realization of many phenomena and functionalities unavailable through use of naturally occurring materials. Many basic metamaterial structures, such as metal split-ring resonators [9], exhibit a birefringence suitable for polarization conversion [10], have been mostly investigated in both microwave range and THz range. In recent years, exhibiting extraordinary responses in various desired frequency regime, metamaterials have been widely applied as an effective means to manipulate polarization of the electromagnetic waves [11,12]. The manipulation of metasurface is highly dependent on the geometric structures of the cells [13]. Therefore, metasurface-based polarizers have been widely studied because they are capable

of flexibly and effectively regulating the polarization state of the THz wave. Grady et al. demonstrated ultrathin, broadband, and highly efficient metamaterial-based THz polarizer that can reflect a linear polarization wave and convert it into a cross polarization one [5]. Liu et al. proposed a broadband THz cross-polarizer operating in transmission mode using a single-layer metasurface [14]. Moreover, an ultra-wideband high-efficiency reflective linear-to-circular (LTC) polarizer based on metasurface at THz frequencies was proposed by Jiang et al [15]. However, the above metasurface-based polarizers, designed by using gold, are restricted in some practical applications due to a lack of reconfigurability.

With the increasing demand for reconfigurable devices, two-dimensional (2D) materials such as graphene and black phosphorus (BP), with the adjustable conductivity, have attracted tremendous attention in the light of the reconfigurable metasurfaces [16,17]. Graphene, with its unique electronic and optical properties, has been widely applied in reconfigurable polarizer. Utilizing the tunability of graphene, an ultra-broadband LTC polarizer and a cross-polarizer are, respectively, present in [18] and [19], and the operating bands can be easily switched to other frequencies. BP, due to its puckered hexagonal honeycomb structure with ridges caused by sp^3 hybridization, offers attractive alternatives to narrow-gap semiconductors for optoelectronics across mid-infrared and THz frequencies [20]. For example, [21] proposed a broadband reflective LTC polarizer in a mid-infrared regime based on monolayer BP (phosphorene) metamaterial. Generally, 2D matearials have been attracting increasing attention as a candidate in the design of THz polarizer. However, their moderate carrier mobility (e.g., 2×10^5 cm^{2}V^{-1}s^{-1} at 5 K for graphene [22] and 5×10^5 cm^{2}V^{-1}s^{-1} at 30 K for BP [23]) are still a limitation in their application.

Because of the ultrahigh mobility of 9×10^6 cm^{2}V^{-1}s^{-1} at 5 K [24,25], recently, Bulk Dirac semimetals (BDSs) showed promise in the design potential of a THz polarizer. For instance, Dai et al. investigated a broadband tunable THz cross-polarizer based on BDSs [26]. With increasing E_F, the cross-conversion bandwidth is widened and exhibits a blue-shift. Furthermore, they proposed a dynamically tunable broadband LTC polarizer based on metasurface [27], where the proposed metasurface consists of a center-cut cross-shaped metallic patterned structure with a sandwiched BDS ribbon. Both of the above-mentioned designs in [26] and [27] achieve the adjustable performance in terms of frequency, but the absence of polarization reconfigurability is still a limitation to their application.

In this paper, we present a BDS-based broadband reconfigurable polarizer operating in the THz region. By controlling the Fermi energy of the BDS, the proposed polarizer can dynamically switch the conversion mode between cross polarization and LTC polarization without reoptimizing the structures. The LTC polarization conversion with AR < 3 dB and cross-polarization conversion with PCR > 80% opera at an identical frequency band with a relative bandwidth (RBW) of 64%. Then, the physical mechanism and the verification were investigated by the decomposition of two orthogonal components and the interference theory, respectively.

2. Materials and Methods

The schematic of the proposed metasurface-based polarizer is shown in Figure 1. The polarizer consists of a double-arc BDS structure with a thickness of 0.17 μm, a dielectric layer with permittivity $\varepsilon_r = 3.0$ and a loss tangent $\tan\theta = 0.001$, and a fully reflective gold mirror. The circular-polarized (CP) wave or *x*-polarized (XP) wave can be reflected when the *y*-polarized (YP) wave is incident on the polarizer. The geometric parameters of the polarizer include unit length $L = 94.0$ μm, dielectric thickness $h = 50.0$ μm, the distance from the center of the arc to the edge of the cell $a = 22.0$ μm, outer radius $R_o = 70.7$ μm, inner radius $R_i = 57.7$ μm, and half of the angle corresponding to the outer arc $\alpha = 31.5°$ and inner arc $\beta = 25.2°$.
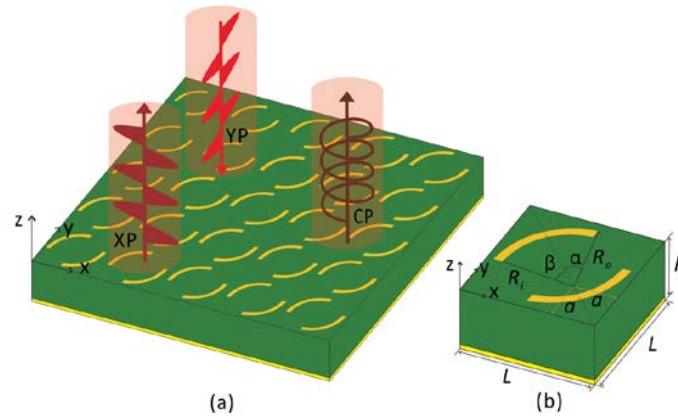
Figure 1. Design of the polarizer, (**a**) 5×5 unit structure diagram, (**b**) A unit cell diagram.

At the long wavelength limit (the local response approximation), the longitudinal dynamic conductivity of the Dirac 3D electron gas in BDSs can be calculated by the Kubo formalism [28]:

$$
\begin{aligned}
\sigma(\omega) &= \sigma_{\text{intra}} + \sigma_{\text{inter}} \\
\sigma_{\text{intra}} &= \frac{ie^2}{\hbar} \frac{gk_F}{6\pi^2\Omega} \left(1 + \frac{\pi^2}{3}\left(\frac{T}{E_F}\right)^2\right) \\
\sigma_{\text{inter}} &= \frac{ie^2 g\omega}{3\pi^2 \hbar v_F} \left[-\frac{\pi i}{2} \frac{G(\hbar\omega/2)}{4} + \int_0^\infty \left(\frac{G(E) - G(\hbar\omega/2)}{\hbar^2\omega^2 - E^2}\right) E dE\right]
\end{aligned}
\tag{1}
$$

where σ_{intra} and σ_{inter} represent the intraband and interband contributions, respectively. $\hbar$ and g are respectively the reduced Planck constant and the degeneracy factor, E_F, v_F, and k_F are respectively the Fermi level, Fermi speed, and Fermi Momentum, moreover k_F is calculated by $E_F/\hbar v_F$. $G(E) = n(-E) - n(E)$, and $n(E)$ is the Fermi distribution function. In the case of electron-hole (e−h) symmetry of the Dirac spectrum for the nonzero temperature T, the real and imaginary parts of the longitudinal dynamic conductivity of the Dirac semimetal can be expressed as

$$
\text{Re}\sigma(\Omega) = \frac{e^2}{\hbar} \frac{gk_F}{24\pi} G(\Omega - 2)
\tag{2}
$$

$$
\text{Im}\sigma(\Omega) = \frac{e^2}{\hbar} \frac{gk_F}{24\pi^2} \left[\frac{4}{\Omega}\left(1 + \frac{\pi^2}{3}\left(\frac{T}{E_F}\right)^2\right) + 8\Omega \int_0^{\varepsilon_c} \left(\frac{G(\varepsilon) - G(\Omega/2)}{\Omega^2 - 4\varepsilon^2}\right)\varepsilon d\varepsilon\right]
\tag{3}
$$

In more detail, with a low-temperature limit, such as $T \ll E_F$, in the electron-hole (e−h) symmetry of the Dirac spectrum, the complex conductivity is expressed as [28]

$$
\text{Re}\sigma(\Omega) = \frac{e^2}{\hbar} \frac{gk_F}{24\pi} \Omega\theta(\Omega - 2)
\tag{4}
$$

$$
\text{Im}\sigma(\Omega) = \frac{e^2}{\hbar} \frac{gk_F}{24\pi} \left[\frac{4}{\Omega} - \Omega\text{Ln}\left(\frac{4\varepsilon_c^2}{|\Omega^2 - 4|}\right)\right]
\tag{5}
$$

where $\Omega = \hbar\omega/E_F + jv_F/(E_F k_F \mu)$ is the normalized frequency, and the relative permittivity of the BDSs can be expressed as $\varepsilon = \varepsilon_b + i\sigma/\omega\varepsilon_0$, where $\varepsilon_b = 1$ is the effective background dielectric constant and ε_0 is the permittivity of vacuum.

Table 1 shows some representative BDSs with various ε_b and g. In this study, AlCuFe was selected as the BDS material and its dynamic conductivity is shown in Figure 2, where $g = 40$, $E_c = 3$, $v_F = 106$ m/s, and $\mu = 3 \times 10^4$ cm^{2}V^{-1}s^{-1}. The hatched regions indicate the normalized frequency range for the THz gap, $\hbar\omega/E_F \approx 1.30$, 0.87, and 0.65 corresponding to $E_F = 30$ meV, 45 meV, and 65 meV when $f = 10$ THz. It is clear that in the low frequency of THz gap, the real component can be neglected because it is far lower than the imaginary component.

Table 1. Representative Bulk Dirac semimetals (BDSs) with different ε_b and g.

Dirac Semimetal	ε_b	g
AlCuFe	1	40
TaAs	6.2	24
Eu2IrO7	6.2	24
Na3Bi	12	4
Cd3As2	12	4
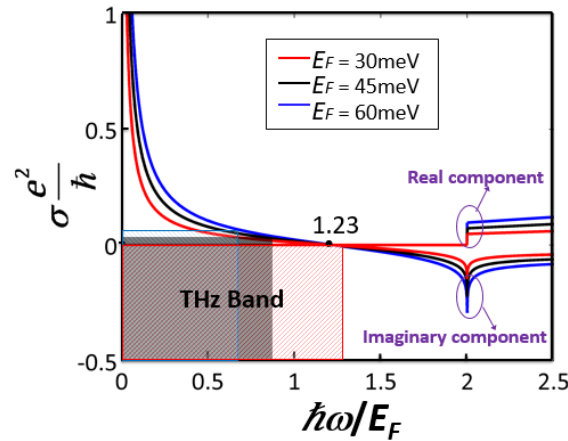
Figure 2. Normalized frequency-dependent conductivity of BDS.

This periodic structure is emulated by CST Microwave Studio, in which the infinite periodic array is simulated by the utilization of the periodic boundary conditions in x and y directions. Because of the anisotropy of the proposed metasurface, the x and y polarized components are simultaneously produced, with a YPincident wave, in the reflective wave. Therefore, the conversion principle can be clearly demonstrated by the reflective wave expression of $E_r = r_{xy}\exp(j\varphi_{xy})E_{yi}e_x + r_{yy}\exp(j\varphi_{yy})E_{yi}e_y$, where r_{xy} and r_{yy} are, respectively, the magnitudes of the reflection coefficient for y-to-x and y-to-y polarization conversion, φ_{xy} and φ_{yy} are the corresponding phases. Then, phase difference is defined by $\Delta\varphi = \varphi_{yy} - \varphi_{xy}$. When $r_{xy} = r_{yy} = \sqrt{2}/2$ and $\Delta\varphi = 2n \pm \pi/2$ (*n* is an integer), the perfect LTC polarization conversion is brought; with "−" and "+", the reflected waves are, respectively, the right-hand circular polarization (RHCP) wave and the left-hand circular polarization (LHCP) wave. On contrast, the total cross polarization conversion is brought with $r_{xy} = 1$ and $\Delta\varphi = 2n \pm \pi$ [29]. In order to achieve a high efficiency of polarization conversion, the reflection coefficient amplitudes should be controlled as highly as possible within the demanded $\Delta\varphi$.

3. Results and Discussions

With $E_F = 30$ meV of BDS (AlCuFe), the reflection coefficient magnitudes and the phase difference are shown in Figure 3a. One can observe that $r_{xy} \approx r_{yy} \approx \sqrt{2}/2$ and $\Delta\varphi \approx -90°$ or 270° in the frequency range of 0.51–1.06 THz. Similarly, $\Delta\varphi \approx 90°$ in the range of 0.41–0.46 THz with $r_{xy} \approx r_{yy} \approx \sqrt{2}/2$. The results indicate that the incident linear polarized wave is converted into a RHCP wave within a broadband and a LHCP wave within a narrow band. When the E_F is adjusted to 45 meV, $r_{yy} < 0.3$ and $r_{xy} > 0.9$ in the frequency range of 0.57–1.12 THz, as shown in Figure 3b, which means that the YPincident waves are converted into the cross-polarized reflected waves by the polarizer.
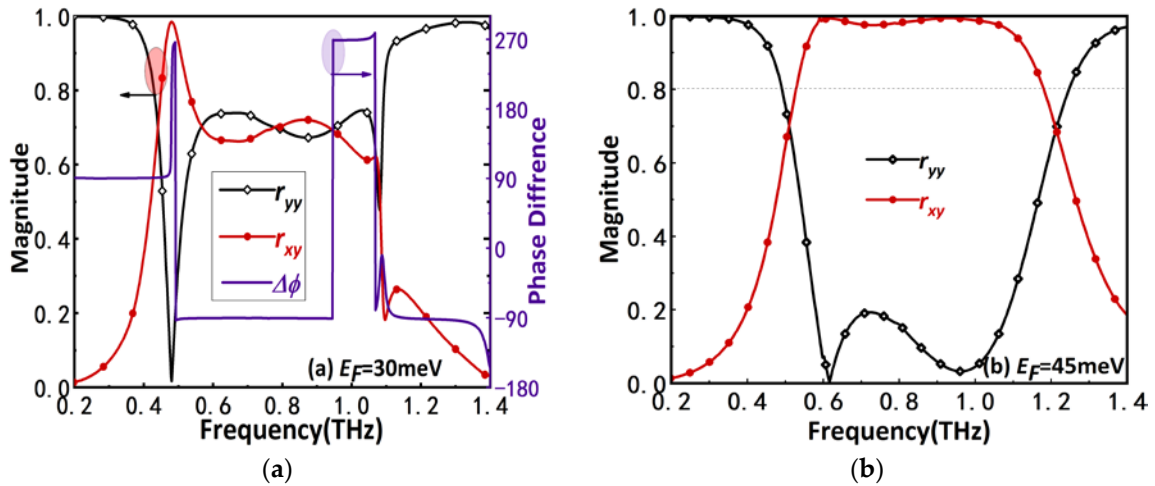
Figure 3. Reflective coefficients ryy and rxy with the Fermi energy of (**a**) 30 meV and (**b**) 45 meV.

For the LTC polarization conversion, the remarkable characteristic can also be measured by the efficiency $\eta_{LTC} = r_{xy}{}^2 + r_{yy}{}^2$ and the axial ratio, AR = 10 lg(tanβ) with β = arcsin(V/I)/2 [13], obtained from the stokes parameter in Equation (3) [30]. In contrast, for cross-polarization conversion, the cross polarization conversion efficiency is estimated as $\eta_{cross} = r_{xy}{}^2$ and PCR = $r_{xy}{}^2/(r_{xy}{}^2 + r_{yy}{}^2)$ is defined to further investigate the performance [31].

$$
\begin{aligned}
I &= r_{yy}{}^2 + r_{xy}{}^2 \\
Q &= r_{yy}{}^2 - r_{xy}{}^2 \\
U &= 2r_{yy}r_{xy}\cos\Delta\phi \\
V &= 2r_{yy}r_{xy}\sin\Delta\phi
\end{aligned}
\tag{6}
$$

For different E_F, the calculated PCR and AR are presented in Figure 4a. One can observe that the relative bandwidth (RBW) with PCR > 0.8 reaches 71% and the RBW of RHCP and LHCP with AR < 3 dB are, respectively, 71% and 11%. More significantly, a RBW of 64% is obtained in the identical frequency band; moreover, both η_{LTC} and η_{cross} are greater than 90%, as shown in Figure 4b, which indicates the high performance of the proposed polarizer.
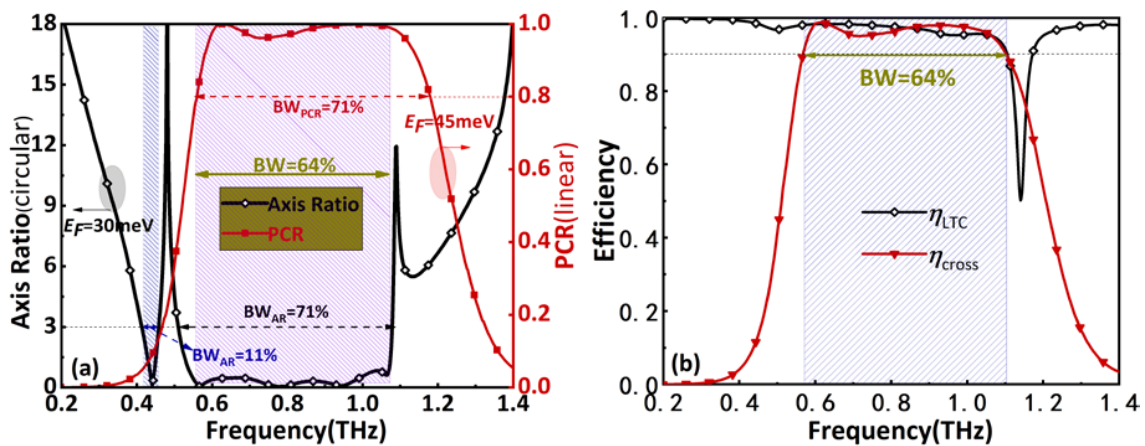

Figure 4. (**a**) AR and PCR and (**b**) efficiencies.

In addition, the AR and PCR of the proposed design as the function of incident angle (θ) and frequency are simulated, as shown in Figure 5a,b. It is clear that in the θ range of 0° and 50°, the BWs of AR < 3 dB and PCR > 0.8 are almost invariant. One can obtain the robustness of the proposed polarizer in case of oblique incidence.
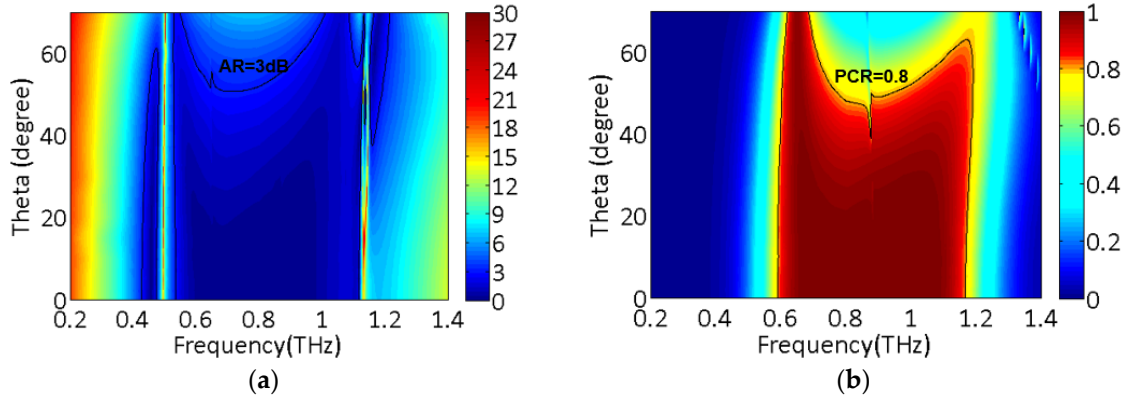
Figure 5. Frequency and Theta-dependent (**a**) AR and (**b**) PCR.

With various E_F, the conductivity of the BDS (AlCuFe) is adjustable, which causes the reconfigurability of the proposed BDS-based polarizer. Therefore, it is reasonable to study the effects of various E_F on the conversion performance. The AR for E_F = 25, 30, and 35 meV are shown in Figure 6a. It can be seen that an optimal LTC polarization conversion performance can be obtained when E_F = 30 meV. Figure 6b shows the PCR gradually improves with increasing E_F from 25 to 45 meV, and the operating frequency band exhibits a blue shift. Furthermore, the bandwidth of PCR becomes narrower gradually with increasing E_F, which will lead to the degradation of the conversion performance. From Figure 6, one can conclude that the design polarizer achieves the optimized performances of cross polarization conversion with E_F = 45 meV and the LTC polarization conversion with E_F = 30 meV.
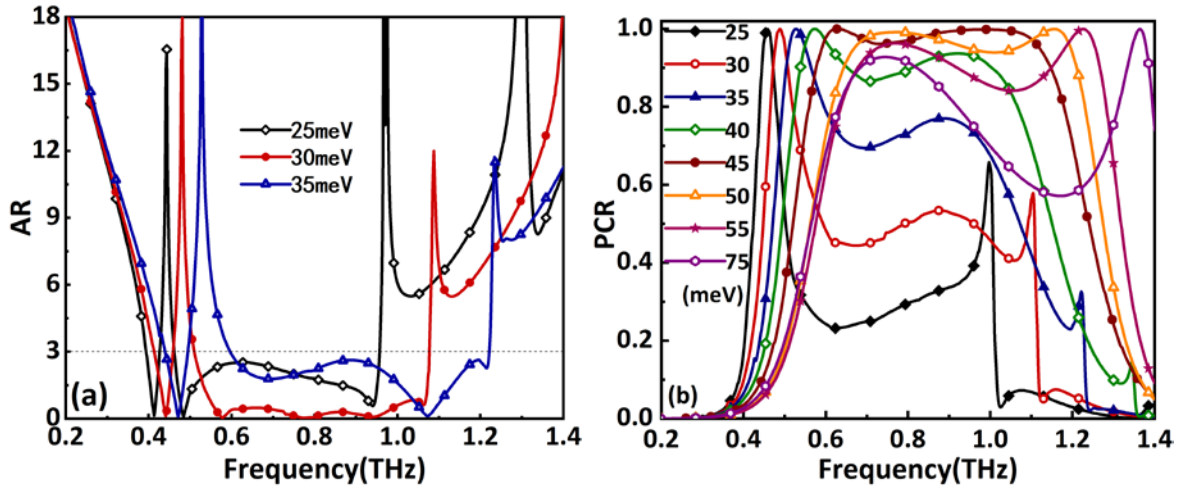

Figure 6. (**a**) AR and (**b**) PCR related to E_F.

4. Mechanism and Verification

In order to analyze the physical mechanism of polarization conversion, the incident YP wave is decomposed into two orthogonal components presenting in Figure 7a, wherein the u-v coordinate system is obtained by rotating the x−y coordinate system counterclockwise for 45° [29]. The incident wave is set to be a YP wave propagating in the -z direction and can be decomposed into

$$E_i = E_i e^{jkz} e_y = \frac{E_i e^{jkz} e_u}{\sqrt{2}} + \frac{E_i e^{jkz} e_v}{\sqrt{2}} \tag{7}$$

$$E_r = \frac{\left(r_{uu} E_i e^{j(-kz+\phi_{uu})} + r_{uv} E_i e^{j(-kz+\phi_{uv})}\right) e_u}{\sqrt{2}} + \frac{\left(r_{vu} E_i e^{j(-kz+\phi_{vu})} + r_{vv} E_i e^{j(-kz+\phi_{vv})}\right) e_v}{\sqrt{2}} \tag{8}$$

In the above formula, r_{uu}, r_{vu}, r_{vv}, and r_{uv} represent the reflection coefficient amplitudes for the polarization conversion of $u-u$, $u-v$, $v-v$, and $v-u$ respectively, φ_{uu}, φ_{vu}, φ_{vv} and φ_{uv} represent the corresponding phases. When $r_{vu} = r_{uv} = 0$, $r_{uu} = r_{vv} = r$ and $\Delta\varphi = \varphi_{vv} - \varphi_{uu} = 2n \pm \pi/2$, the reflected wave is expressed as

$$E_r = \frac{rE_i e^{-jkz}\left(e^{j\phi_{uu}}e_u + e^{j(\phi_{uu}+2n\pi\pm\pi/2)}e_v\right)}{\sqrt{2}} \tag{9}$$

It can be seen from Equation (6) that the reflected wave is a CP wave. Moreover, when $r_{vu} = r_{uv} = 0$, $r_{uu} = r_{vv} = r$ and $\Delta\varphi = \varphi_{vv} - \varphi_{uu} = 2n \pm \pi$ the reflected wave is a cross-polarized wave and can be expressed as

$$E_r = \frac{rE_i e^{-jkz}\left(e^{j\phi_{uu}}e_u + e^{j(\phi_{uu}+2n\pi\pm\pi)}e_v\right)}{\sqrt{2}} \tag{10}$$
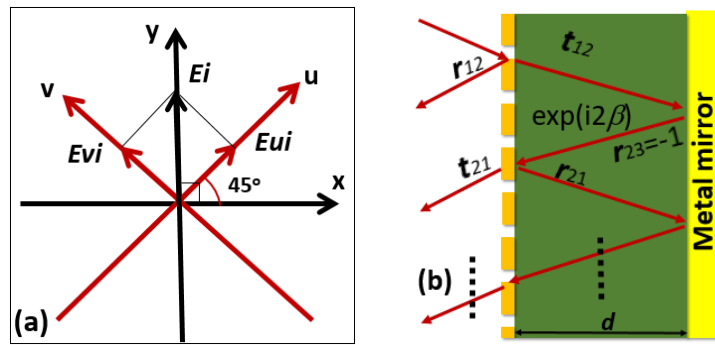

Figure 7. (**a**) u-v coordinate system, (**b**) Multiple reflection interference.

When the u and v components excite simultaneously and $E_F = 30$ meV, as shown in Figure 8a, $r_{uu} = r_{vv} \approx 1$, $r_{vu} = r_{uv} \approx 0$ and $\Delta\varphi = \varphi_{vv} - \varphi_{uu}$ closing to $-90°/270°$ are obtained in the frequency range of 0.5 and 1.08 THz, incidentally $\Delta\varphi$ being approximately $90°$ is obtained in the band of 0.41–0.46 THz, i.e., the reflected waves are respectively RHCP wave and LHCP wave in these two bands. In contrast, when $E_F = 45$ meV, $r_{uu} = r_{vv} \approx 1$, $r_{vu} = r_{uv} \approx 0$ and $\Delta\varphi \approx -180°/180°$ is obtained, as shown in Figure 8b, the cross-polarization conversion is realized. It is observed that the polarization conversions are consistent with that in Figure 3.
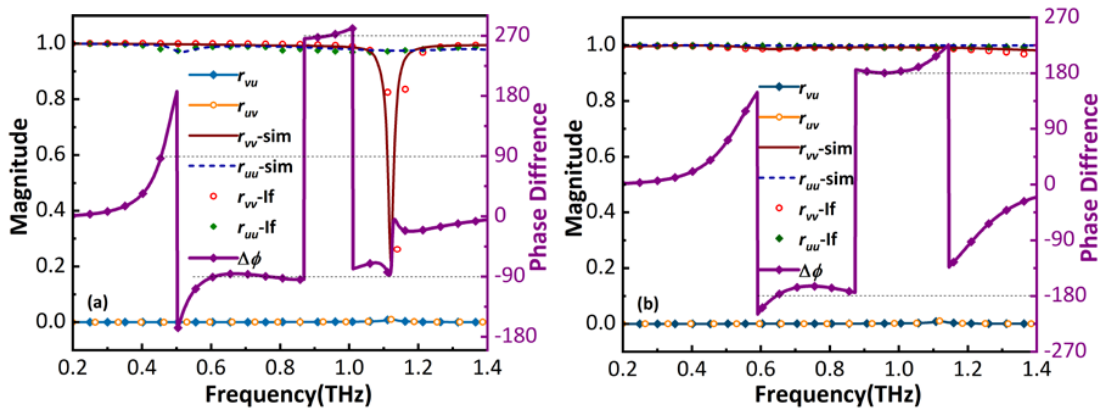

Figure 8. The calculated and simulated reflection coefficients of u- and v-polarized reflected waves. (**a**) LTC polarization conversion, (**b**) Cross-polarization conversion.

The verification can be further elaborated by the interference theory in the $u-v$ coordinate system. As present in Figure 7b, at the double-arc array interface, the incident wave is partially reflected with a reflection coefficient of $r_{12} = r_{12}\exp(i\varphi_{12})$ and transmitted into the substrate with a transmission

coefficient of $t_{12} = t_{12}\exp(i\theta_{12})$. The transmitted wave continues to propagate with a propagation phase $\beta = \sqrt{\varepsilon}kd$ until it reaches the metal mirror, where ε and d are, respectively, the permittivity and the thickness of the substrate, and k is the propagation constant in the substrate. After the reflection at the metal mirror and the addition of another β, partial reflection and transmission occur again at the double-arc interface with coefficients $r_{21} = r_{21}\exp(i\varphi_{21})$ and $t_{21} = t_{21}\exp(i\theta_{21})$. Similarly to the wave propagation in a stratified media, the total reflection is the superposition of the multiple reflections [32]:

$$r = r_{12} - t_{12}t_{21}e^{i2\beta} + t_{12}r_{21}t_{21}e^{i4\beta} - t_{12}r_{21}{}^2t_{21}e^{i4\beta} + \dots \tag{11}$$

$$r = r_{12} - \frac{t_{12}t_{21}e^{i2\beta}}{1 + r_{21}e^{i2\beta}} \tag{12}$$

The results calculated by the interference theory are shown in Figure 8. The reflection coefficients of the LTC polarization conversion and the cross-polarization conversion are consistent with the simulation results, which verities the simulated results of the proposed polarizer.

5. Conclusions

In conclusion, a reconfigurable polarizer based on BDS metasurface is investigated in this paper, and the conversion performance and physical mechanism are analyzed and presented. Our results show that the proposed polarizer achieves a highly efficient linear-to-circular polarization conversion or cross polarization conversion in broadband with different E_F. This design is of great significance in the wide application of metamaterials and the rapid development of THz technology.

References

1. Dean, P.; Lim, Y.L. Terahertz sensing through self-mixing in a quantum cascade laser. *Opt. Lett.* **2011**, *36*, 2587–2589. [CrossRef] [PubMed]
2. Chan, W.L.; Deibel, J.; Mittleman, D.M. Imaging with terahertz radiation. *Rep. Prog. Phys.* **2007**, *70*, 1325–1379. [CrossRef]
3. Koenig, S.; Lopez-Diaz, D.; Antes, J. Wireless sub-THz communication system with high data rate. *Nat. Photonics* **2013**, *7*, 977–981. [CrossRef]
4. Kleine-Ostmann, T.; Nagatsuma, T. A Review on Terahertz Communications Research. *J. Infrared Millim. Terahertz Waves* **2011**, *32*, 143–171. [CrossRef]
5. Grady, N.K.; Heyes, J.E.; Chowdhury, D.R. Terahertz Metamaterials for Linear Polarization Conversion and Anomalous Refraction. *Science* **2013**, *340*, 1304–1307. [CrossRef]
6. Sinchuk, K.; Dudley, R.; Graham, J.D. Tunable negative group index in metamaterial structures with large form birefringence. *Opt. Express* **2010**, *18*, 463–472. [CrossRef]
7. Noda, S.; Yokoyama, M.; Imada, M. Polarization mode control of two-dimensional photonic crystal laser by unit cell structure design. *Science* **2001**, *293*, 1123–1125. [CrossRef]
8. Kanda, N.; Konishi, K.; Kuwatagonokami, M. Terahertz wave polarization rotation with double layered metal grating of complimentary chiral patterns. *Opt. Express* **2007**, *15*, 11117–11125. [CrossRef]

9. Pendry, J.B.; Holden, A.J.; Robbins, D.J. Magnetism from conductors and enhanced nonlinear phenomena. IEEE Transactions on Microwave Theory Techniques. *IEEE Trans. Microw. Theory* **1997**, *47*, 2075–2084. [CrossRef]

10. Hao, J.; Yuan, Y.R.; Li, X. Manipulating Electromagnetic Wave Polarizations by Anisotropic Metamaterials. *Phys. Rev. Lett.* **2007**, *99*, 063908. [CrossRef]

11. Yu, N.; Capasso, F. Flat optics with designer metasurfaces. *Nat. Mater.* **2014**, *13*, 139–150. [CrossRef] [PubMed]

12. Zhao, Y.; Alù, A. Manipulating light polarization with ultrathin plasmonic metasurfaces. *Phys. Rev. B* **2011**, *84*, 205428. [CrossRef]

13. Zhang, M.; Zhang, W.; Liu, A.Q. Tunable Polarization Conversion and Rotation based on a Reconfigurable Metasurface. *Sci. Rep.* **2017**, *7*, 12068. [CrossRef] [PubMed]

14. Liu, W.; Chen, S.; Li, Z. Realization of broadband cross-polarization conversion in transmission mode in the terahertz region using a single-layer metasurface. *Opt. Lett.* **2015**, *40*, 3185–3188. [CrossRef]

15. Jiang, Y.N.; Wang, L.; Wang, J. Ultra-wideband high-efficiency reflective linear-to-circular polarization converter based on metasurface at terahertz frequencies. *Opt. Express* **2017**, *25*, 27616–27623. [CrossRef]

16. Katsnelson, M.I.; Novoselov, K.S.; Geim, A.K. Chiral tunnelling and the Klein paradox in graphene. *Nat. Phys.* **2006**, *2*, 620–625. [CrossRef]

17. Low, T.; Rodin, A.S.; Carvalho, A.; Jiang, Y.; Wang, H. Tunable optical properties of multilayer black phosphorus thin films. *Phys. Rev. B* **2014**, *90*, 075434. [CrossRef]

18. Zeng, L.; Huang, T.; Liu, G.B. A tunable ultra-broadband linear-to-circular polarization converter containing the graphene. *Opt. Commun.* **2019**, *436*, 7–13. [CrossRef]

19. Luo, S.; Li, B.; Yu, A. Broadband tunable terahertz polarization converter based on graphene metamaterial. *Opt. Commun.* **2018**, *413*, 184–189. [CrossRef]

20. Koenig, S.P.; Doganov, R.A.; Schmidt, H. Electric field effect in ultrathin black phosphorus. *Appl. Phys. Lett.* **2014**, *104*, 103106. [CrossRef]

21. Jiang, Y.; Zhao, H.; Wang, L.; Wang, J. Broadband linear-to-circular polarization converter based on phosphorene metamaterial. *Opt. Mater. Express* **2019**, *5*, 2088–2097. [CrossRef]

22. Bolotin, K.I.; Sikes, K.J.; Jiang, Z. Ultrahigh electron mobility in suspended graphene. *Solid State Commun.* **2008**, *146*, 351–355. [CrossRef]

23. Xia, F.; Wang, H.; Xiao, D. Two-dimensional material nanophotonics. *Nat. Photonics* **2015**, *8*, 899–907. [CrossRef]

24. Liang, T.; Gibson, Q.; Ali, M.N. Ultrahigh mobility and giant magnetoresistance in the Dirac semimetal Cd_3As_2. *Nat. Mater.* **2014**, *14*, 280–284. [CrossRef]

25. Jiang, Y.; Wan, X.; Wang, J. Tunable terahertz absorber based on bulk-Dirac-semimetal metasurface. *IEEE Photonics J.* **2018**, *10*, 4600607. [CrossRef]

26. Dai, L.; Zhang, Y.; Zhang, H. Broadband tunable terahertz cross-polarization converter based on Dirac semimetals. *Appl. Phys. Express* **2019**, *12*, 075003. [CrossRef]

27. Dai, L.; Zhang, Y.; Guo, X. Dynamically tunable broadband linear-to-circular polarization converter based on Dirac semimetals. *Opt. Mater. Express* **2018**, *10*, 3238–3249. [CrossRef]

28. Kotov, O.V.; Lozovik, Y.E. Dielectric response and novel electromagnetic modes in three-dimensional Dirac semimetal films. *Phys. Rev. B* **2016**, *93*, 235417. [CrossRef]

29. Zahn, M. *Electromagnetic Field Theory: A Problem Solving Approach*; Krieger Publishing Company: Malabar, FL, USA, 2003; pp. 135–139.

30. Li, Y.; Zhang, J.; Qu, S. Achieving wide-band linear-to-circular polarization conversion using ultra-thin bi-layered metasurfaces. *J. Appl. Phys.* **2015**, *117*, 044501. [CrossRef]

31. Winkler, S.A.; Wei, H.; Bozzi, M. Polarization Rotating Frequency Selective Surface Based on Substrate Integrated Waveguide Technology. *IEEE Trans. Antennas Propag.* **2010**, *58*, 1202–1213. [CrossRef]

32. Chen, H.T. Interference theory of metamaterial perfect absorbers. *Opt. Express* **2012**, *20*, 7165–7172. [CrossRef]